ACS APPLIED MATERIALS & INTERFACES

Research Article

www.acsami.org

Core–Shell Structural CdS@SnO_2 Nanorods with Excellent Visible-Light Photocatalytic Activity for the Selective Oxidation of Benzyl Alcohol to Benzaldehyde

Ya Liu, Ping Zhang, Baozhu Tian,* and Jinlong Zhang*

Key Lab for Advanced Materials and Institute of Fine Chemicals, East China University of Science and Technology, 130 Mei Long Road, Shanghai 200237, People's Republic of China

Supporting Information

ABSTRACT: Core–shell structural CdS@SnO_2 nanorods (NRs) were fabricated by synthesizing SnO_2 nanoparticles with a solvent-assisted interfacial reaction and further anchoring them on the surface of CdS NRs under ultrasonic stirring. The morphology, composition, and microstructures of the obtained samples were characterized by field-emission scanning electron microscopy, transmission electron microscopy, X-ray diffraction, X-ray photoelectron spectroscopy, and nitrogen adsorption–desorption. It was found that SnO_2 nanoparticles can be tightly anchored on the surface of CdS NRs, and the thickness of SnO_2 shells can be conveniently adjusted by simply changing the addition amount of SnO_2 quantum dots. UV–vis diffuse reflectance spectrum indicated that SnO_2 shell layer also can enhance the visible light absorption of CdS NRs to a certain extent. The results of transient photocurrents and photoluminescence spectra revealed that the core–shell structure can effectively promote the separation rate of electron–hole pairs and prolong the lifetime of electrons. Compared with the single CdS NRs, the core–shell structural CdS@SnO_2 exhibited a remarkably enhanced photocatalytic activity for selective oxidation of benzyl alcohol (BA) to benzaldehyde (BAD) under visible light irradiation, attributed to the more efficient separation of electrons and holes, improved surface area, and enhanced visible light absorption of core–shell structure. The radical scavenging experiments proved that in acetonitrile solution, $\cdot O_2^-$ and holes are the main reactive species responsible for BA to BAD transformation, and the lack of ·OH radicals is favorable to obtaining high reaction selectivity.

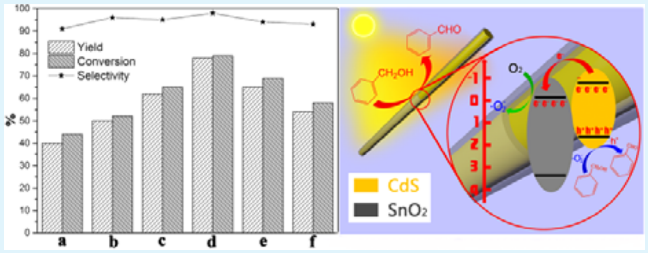

KEYWORDS: *CdS@SnO_2, selective oxidation, benzyl alcohol, benzaldehyde, photocatalytic activity*

1. INTRODUCTION

Core–shell nanocomposite photocatalysts have attracted much attention for their potential applications in solving serious environmental and energy crises owing to their improved surface, optical, electronic, and photocatalytic properties compared with single materials.[1−5] Until now, they have been researched in a wide variety of fields, such as environment remediation,[6,7] hydrogen production,[8,9] and selective organic synthesis.[10,11] Indisputably, the heterostructure of core–shell semiconductor materials can facilitate the separation of photogenerated electron–hole pairs by creating a staggered band gap offset and thus making the photogenerated electrons in one semiconductor be injected into the lower-lying conduction band of the second semiconductor. Therefore, the core–shell heterostructure photocatalysts with suitable band gap offsets often exhibit enhanced photocatalytic performances compared to those of the single photocatalyst.

In addition to the core–shell structure, the photocatalytic materials with one-dimensional (1D) nanostructure have also attracted a great deal of research interest for their unique structural and electronic properties in recent years.[11−13] Compared with nanoparticles and bulk materials, 1D structural materials have several advantages as photocatalysts:[14,15] First, the 1D geometrical structure can provide a large aspect-ratio, which may enhance the capacity of light absorption. Second, the separation efficiency of electron–hole pairs can be improved due to their considerably higher electron mobility and straight transport pathway. Third, 1D nanomaterials can be easily recycled without the decrease of photocatalytic activity.[12] For instance, Zhang et al. synthesized N,F-codoped TiO_2 nanowires by a hydrothermal route and found that N,F-codoped TiO_2 nanowires showed much higher photocatalytic performance for the degradation of atrazine under UV and visible light irradiation in comparison with N,F-codoped TiO_2 nanoparticles.[16]

Due to so many advantages of core–shell and 1D structural materials, the synthesis and photocatalytic performance of 1D core–shell structural materials have gradually become one of research hotspots.[17−20] However, these studies mainly focused on "nonselective" degradation of organic pollutants[17,18] and

Received: March 6, 2015
Accepted: June 9, 2015
Published: June 9, 2015

DOI: 10.1021/acsami.5b04128
ACS Appl. Mater. Interfaces 2015, 7, 13849−13858

water splitting.[19,20] Research works on "selective" photocatalytic oxidation reaction with 1D core−shell structural materials have rarely been reported. Oxidation of alcohols to aldehydes is an important organic reaction because carbonyl compounds are widely used as the intermediates for many fragrances, drugs, and vitamins.[21−23] However, traditional organic synthesis of aldehydes from corresponding alcohols not only involves toxic or corrosive oxidants (such as ClO^-, Cr^{4+}, and Cl_2), but also consumes a great deal of energy to provide the temperature and pressure needed by the reactions.[24,25] To overcome these drawbacks, tremendous efforts have been devoted in the past decade.[21−27] Among the various available strategies, utilizing semiconductor photocatalysts for organic synthesis has attracted much attention due to the several advantages, such as energy efficiency, environmental friendliness, reusability, and durability. However, the rapid recombination of photogenerated electron−hole pairs always results in a relatively low efficiency in photocatalytic reactions. Therefore, optimizing the charge carrier transfer process to inhibit the recombination of electrons and holes is an important theme for selective organic syntheses using solar energy in future.[28]

Against this background, we herein explore a facile procedure to fabricate core−shell structural CdS@SnO_2 nanorods (NRs) for selective oxidation of alcohols to aldehydes, in which SnO_2 quantum dots (QDs) were prepared by a solvent-assisted interfacial reaction and further anchored on the surface of CdS NRs under ultrasonic stirring. The morphology, composition, and structures of the obtained samples were characterized by the means of field-emission scanning electron microscopy (FESEM), transmission electron microscopy (TEM), X-ray diffraction (XRD), X-ray photoelectron spectroscopy (XPS), and nitrogen adsorption−desorption. Meanwhile, UV−vis diffuse reflectance spectrum (DRS), transient photocurrents, and photoluminescence (PL) spectrum tests were carried out to investigate the influence of SnO_2 shell layer on the light absorption and photoelectric properties of CdS NRs. Photocatalytic oxidation of benzyl alcohol (BA) was selected as a probe reaction to evaluate the reactive activity and selectivity of CdS@SnO_2 NRs. Moreover, the reactive species were studied by radical-trapping experiments.

2. EXPERIMENTAL SECTION

2.1. Chemicals. Sodium diethyldithiocarbamate ($NaS_2CNEt_2 \cdot 3H_2O$), cadmium chloride ($CdCl_2 \cdot 2.5H_2O$), $SnCl_4 \cdot 5H_2O$, chloroform ($CHCl_3$), ethylenediamine (EDA), and ethanol (C_2H_5OH) were purchased from Sinopharm Chemical Reagent Co., Ltd. (Shanghai, China). All chemicals were analytical grade and used directly without further purification.

2.2. Fabrication of Core−Shell Structural CdS@SnO_2 NRs. Core−shell structural CdS@SnO_2 NRs were fabricated via a facile two-step method:

2.2.1. Synthesis of CdS NRs. CdS NRs were synthesized by a modified method.[29] In a typical procedure, 1.686 g of $Cd(S_2CNEt_2)_2$ was beforehand prepared by a stoichiometric precipitation reaction between $NaS_2CNEt_2 \cdot 3H_2O$ and $CdCl_2 \cdot 2.5H_2O$ in deionized water. Then, the obtained precipitation was dispersed in 60 mL of EDA and further transferred into a 100 mL Teflon-lined stainless steel autoclave. After the hydrothermal reaction was maintained at 180 °C for 24 h, the autoclave was cooled to room temperature. A yellowish precipitate was collected and washed with absolute ethanol and deionized water for several times to remove the residual organic solvents. Finally, the obtained product was dried in an oven at 60 °C for 8 h.

2.2.2. Preparation of SnO_2 Quantum Dots (QDs). SnO_2 quantum dots were synthesized by a one-step carrier solvent-assisted interfacial reaction method at room temperature.[30] The detailed procedures are as follows: First, 186.1 mg of $SnCl_4 \cdot 5H_2O$ was dissolved in 4 mL of ethanol and subsequently mixed with 4 mL of $CHCl_3$ solution. Then, 8 mL of water was added into the above solution to produce an interface between water and $CHCl_3$ because they are immiscible. Since $SnCl_4 \cdot 5H_2O$ is diffluent in ethanol and insoluble in chloroform as well as ethanol has higher affinity toward water than chloroform, ethanol will transfer from the chloroform domain to water domain, together with $SnCl_4$ precursor. At last, $SnCl_4$ will hydrolyze in the interface of $CHCl_3$ and water to produce SnO_2 QDs. By adjusting the reaction time and temperature, the particle size of SnO_2 quantum dots can be tuned. Here, the reaction temperature and time were 30 °C and 2 h, respectively.

2.2.3. Preparation of Core−Shell Structural CdS@SnO_2 NRs. Core−shell structural CdS@SnO_2 NRs were fabricated with the following procedures:[30,31] 50 mg of CdS NRs was added into 10 mL of ethanol solution (99.5%), followed by adding a desired amount of SnO_2 QDs. Specifically, the addition amounts of SnO_2 suspension are 0, 0.375, 0.75, 1.125, 1.5, and 1.875 mL, respectively, corresponding to 0, 2.5, 5.0, 7.5, 10, and 12.5 mg of SnO_2 nanoparticles. Then, the mixture was treated under ultrasonic stirring for 2 h at room temperature. The final product was washed with absolute ethanol and deionized water for several times, and dried at 60 °C for 8 h. The obtained samples were denoted as CdS@x%SnO_2, in which x refers to the nominal mass ratio of SnO_2 to CdS in CdS@x%SnO_2. The corresponding samples include CdS, CdS@5%SnO_2, CdS@10%SnO_2, CdS@15%SnO_2, CdS@20%SnO_2, and CdS@25%SnO_2.

2.3. Characterization. The crystalline structures of the samples were analyzed by a Rigaku Ultima IV X-ray diffractometer equipped with a graphite monochromator. The X-ray diffraction (XRD) patterns were recorded at room temperature in the angular range of 10−80° (2θ), using Cu Kα radiation (α = 0.15406 nm), operated at 40 kV and 40 mA. The morphologies of the samples were observed with a field-emission scanning electron microscope (FESEM, FEI NOVA Nano SEM450) and a transmission electron microscope (TEM, JEOL JEM2000EX). The EDS analysis was performed on an EDAX-9100 energy-dispersive spectrometer equipped on the FESEM, while selected area electron diffraction (SAED) pattern was also obtained on the JEOL JEM2000EX TEM. UV−vis diffuse reflectance spectra (DRS) were measured with a SHIMADZU UV-2450 spectroscopy equipped with an integrating sphere assembly, using $BaSO_4$ as the reference material. The data were collected in the range of 400−800 nm. XPS spectra were recorded on a Thermo Fisher ESCALAB 250Xi system with Al Kα radiation, operated at 250 W. The shift of the binding energy scale caused by relative surface charging was corrected by referencing the C 1s level at 284.8 eV. BET surface area (S_{BET}) measurements were carried out by N_2 adsorption−desorption at 77 K using a Micromeritics ASAP2020 instrument. The photoluminescence (PL) spectra and time-resolved fluorescence (TRPL) decays were investigated on an EDINBURGH FLS980 fluorescence spectrophotometer. The actual Cr contents in CdS@SnO_2 and solution were measured by an Agilent 725ES Inductively coupled plasma atomic emission spectrometer.

2.4. Photocatalytic Activity and Photocurrent Measurements. The photocatalytic selective oxidation of BA was performed in a 50 mL three-necked flask at room temperature and oxygen atmosphere (1 bar). A 300 W xenon arc lamp with a UV-cutoff filter ($\lambda \geq 420$ nm) was used as the visible light source to trigger the photocatalytic reaction. Acetonitrile, a cheaper and less toxic solvent, was selected as the reaction medium for BA selective oxidation. For each measurement, 50 mg of as-synthesized catalyst was dispersed in the mixed solution of acetonitrile (20 mL) and BA solution (208 μL, 2 mmol). Prior to light irradiation, the mixture was stirred for 1 h in the dark to attain the adsorption−desorption equilibrium for BA and dissolved oxygen on the surface of photocatalyst. At a given time interval, about 4 mL of suspension was withdrawn and centrifuged (12000 rmp, 15 min) to remove the remained particles. The concentrations of BA and BAD were measured with a SHIMADZU SPD-M20A high-performance liquid chromatograph (HPLC). The

DOI: 10.1021/acsami.5b04128
ACS Appl. Mater. Interfaces 2015, 7, 13849−13858

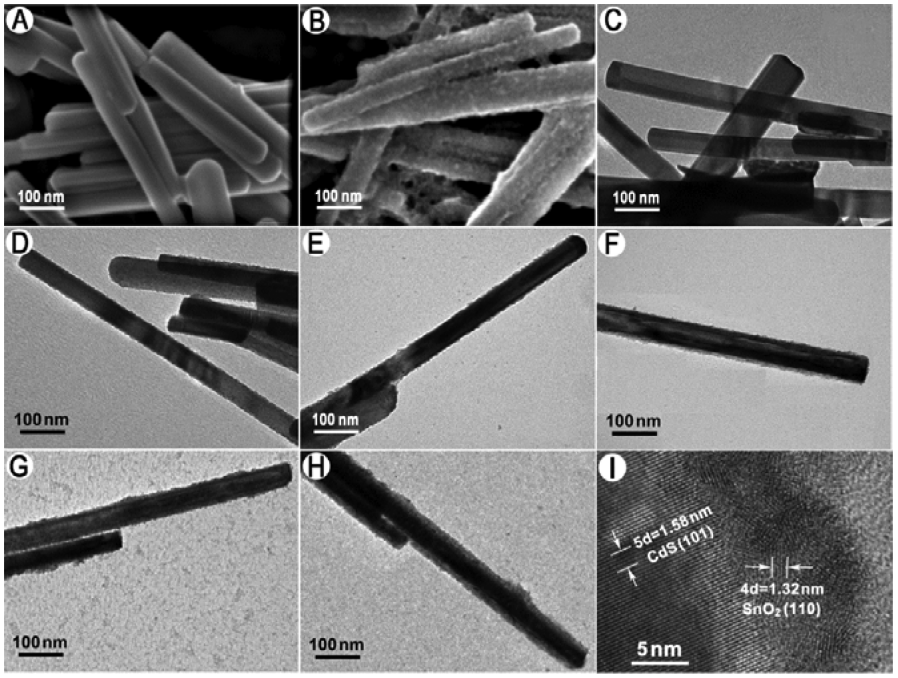

Figure 1. FESEM images of (A) CdS and (B) CdS@15%SnO_2. TEM images of (C) CdS, (D) CdS@5%SnO_2, (E) CdS@10%SnO_2, (F) CdS@15%SnO_2, (G) CdS@20%SnO_2, and (H) CdS@25%SnO_2. (I) HRTEM image of CdS@10%SnO_2.

conversion rate of BA, the yield of BAD, and reaction selectivity were calculated with the following equations:

$$\text{BA conversion } (\%) = \frac{(C_0 - C_1)}{C_0} \times 100$$

$$\text{BAD yield } (\%) = \left(\frac{C_2}{C_0}\right) \times 100$$

$$\text{selectivity } (\%) = \frac{C_2}{(C_0 - C_1)} \times 100$$

Here, C_0 is the initial concentration of BA; C_1 and C_2 are the concentrations of BA and BAD, respectively, after the photocatalytic reactions.[32]

The photocurrents were measured with an electrochemical station (ZAHNER, Germany) in a standard three-electrode system, using the sample as the working electrode with an active area of 1.0 cm^2, a Pt foil as the counter electrode, a saturated calomel electrode (SCE) as the reference electrode, and 0.5 M Na_2SO_4 as the electrolyte. A 300 W Xe arc lamp with a UV cutoff filter ($\lambda \geq 420$ nm) was used as the visible light source.

3. RESULTS AND DISCUSSION

3.1. Morphology and Crystal Structure. The morphological structures of CdS and core−shell structural CdS@SnO_2 NRs were observed with FESEM and TEM. Figure 1A,B shows the FESEM images of CdS and CdS@15%SnO_2. The length of as-prepared CdS NRs is in the range of 0.3−1 μm while their diameter varies from 30 to 80 nm. Different from the smooth surface of CdS NRs (Figure 1A), the surface of CdS@15%SnO_2 NRs becomes rougher (Figure 1B), indicating that SnO_2 QDs have been successfully loaded on the surface of CdS NRs. The self-assembly of CdS@SnO_2 core−shell structure is probably relative to the force of minimizing surface free energy and intermolecular force between CdS NRs and SnO_2 QDs.[33] Probably due to the very small particle size, it is easier for QDs to access the defect positions and further anchor on these defect positions when compared with the bigger particles. In addition, the ultrasound irradiation probably plays an important role for promoting the tightly combination between SnO_2 and CdS. First, the ultrasound irradiation can promote the collision and contact between SnO_2 and CdS, which is favorable to the close combination between SnO_2 and CdS. Second, ultrasound irradiation can generate local hotspots where the high temperature and pressure might be favorable to the combination between SnO_2 and CdS.[34]

The chemical composition of CdS@15%SnO_2 NRs was analyzed by EDS technique (Figure S1, Supporting Information), which confirmed that there are Sn, Cd, S, and O elements. The calculated molar ratios of tin to oxygen and Cd to S are 1:1.8 and 1:1.1, respectively, near to their stoichiometric values. Moreover, the actual content of SnO_2 in CdS@15%SnO_2 was analyzed with ICP-AES, to be 12.8 wt %, which is nearly equal to the nominal SnO_2 content in CdS@15%SnO_2 (13.04 wt %), indicating that almost all of the added SnO_2 QDs have been loaded on CdS surface.

Figure 1C−F shows the TEM images of CdS and CdS@SnO_2 NRs with different SnO_2 dosages. When the addition dosage SnO_2 is 5%, only some burrs can be found on the surface of CdS rod (Figure 1C). Further increasing the dosage of SnO_2 to 10%, it can be seen that most part of the CdS rod surface are covered by SnO_2 shell layer while some area is still bare (Figure 1D). When the dosage of SnO_2 reaches 15%, the entire surface of the CdS NRs is homogeneously coated with a uniform SnO_2 shell layer (Figure 1D−F). Additionally, the thickness of the SnO_2 layer exhibits an increase trend with the increase of SnO_2 dosage, indicating that the thickness of SnO_2 shell layer can be conveniently adjusted by changing the addition amount of SnO_2 nanoparticles.

HRTEM analysis was carried out to investigate the crystal structures of CdS and SnO_2 in CdS@10%SnO_2, As shown in Figure 1I, the lattice spacing of outer SnO_2 layer is about 0.331 nm, corresponding to the (110) crystal plane of a tetragonal

DOI: 10.1021/acsami.5b04128
ACS Appl. Mater. Interfaces 2015, 7, 13849−13858

rutile phase.[35] At different positions, the lattice fringes of SnO_2 arrange along different directions, which reveals that SnO_2 shell layer is composed of many individual SnO_2 nanoparticles. As for the CdS nanorod, all of the lattice fringes arrange along a same direction, implying that the CdS nanorod is single crystal structure, which is further confirmed by SAED technology (Figure S2, Supporting Information). The measured lattice spacing is about 0.316 nm, which is well matched to the (101) lattice plane of hexagonal CdS.[36]

The phase composition, purity, and crystallinity of the as-synthesized samples were analyzed by XRD. The XRD pattern of the as-prepared SnO_2 is shown in Figure S3 (Supporting Information), in which all diffraction peaks match well with the characteristic peaks of tetragonal rutile phase SnO_2 (JCPDS 41-1445). The low and broad diffraction peaks imply the low crystallinity and small particle size, which is favorable to loading on CdS surface. As shown in Figure 2a, the uncoated CdS

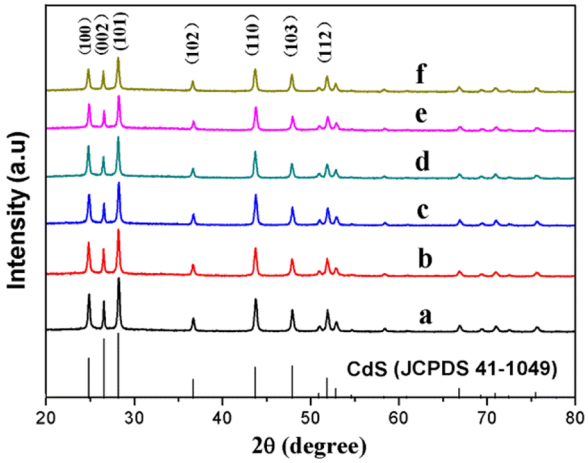

Figure 2. XRD patterns of (a) CdS, (b) CdS@5%SnO_2, (c) CdS@10%SnO_2, (d) CdS@15%SnO_2, (e) CdS@20%SnO_2, and (f) CdS@25%SnO_2.

shows a highly crystalline hexagonal phase with lattice constants of a = 0.4140 nm and c = 0.6719 nm (JCPDS card No. 41-1049). Notably, there is no obvious diffraction peak ascribed to SnO_2 that can be distinguished in all CdS@SnO_2 samples, probably due to the relatively low crystallinity and low content of SnO_2 in CdS@SnO_2 composites. By careful observation, it can be seen that the intensity of CdS diffraction peaks gradually decreases with increasing the content of SnO_2, probably resulting from the influence of SnO_2 shell layer on the X-ray transmission.

3.2. Chemical Composition and Surface Property. The composition and element valence states of CdS@15%SnO_2 were investigated by XPS technique and the results are exhibited in Figure 3. In Figure 3A, there exist two symmetric peaks at 486.85 and 495.25 eV, which should be ascribed to the Sn $3d_{5/2}$ and Sn $3d_{3/2}$, respectively.[37] The gap between Sn $3d_{5/2}$ peak and Sn $3d_{3/2}$ peak is 8.0 eV, consistent with the value of Sn in commercial SnO_2.[37] As shown in Figure 3B, the O 1s profile is broad and asymmetric, implying that there exist at least two different kinds of O species in the sample. According the previous reports,[38,39] the O 1s peak can be fitted into two peaks, in which the peak at 530.7 eV is assigned to the lattice oxygen (O_L) of SnO_2 while the other at 532.0 eV is attributed to the chemisorbed oxygen (O_H) of the surface hydroxyl. Figure 3C shows the Cd 3d XPS spectrum of CdS@15%SnO_2. There are two peaks located at 405.0 and 411.7 eV, which are attributed to Cd $3d_{5/2}$ and Cd $3d_{3/2}$, respectively.[40] In Figure 3D, the S 2p spectrum is composed of two individual peaks of S $2p_{3/2}$ and S $2p_{1/2}$ at 161.6 and 162.8 eV, respectively, indicating that the valence state of element S is −2.[10]

It is known that a larger surface area can offer more adsorption and reactive sites for photocatalytic reactions, leading to an enhancement of reactive activity.[41] Consequently, it is indispensable to investigate the surface area of as-synthesized samples before moving toward the photocatalytic study. In this case, we adopted the nitrogen adsorption−desorption to characterize the surface area and porosity of the as-synthesized samples. As shown in Figure 4, both CdS NRs and CdS@15%SnO_2 display a type IV isotherm with a typical H3 hysteresis loop (at $P/P_0 > 0.80$), implying the presence of interparticle and nonordered mesopores in the samples according to the IUPAC classification.[42] The BET surface areas (S_{BET}) of CdS and different CdS@SnO_2 samples are listed in Table 1, which indicates that the S_{BET} of CdS@SnO_2 gradually increases with the increase of SnO_2 loading amount. This result implies that the core−shell structural CdS@SnO_2 should have a higher adsorption capacity than blank CdS. Accordingly, it can be anticipated that the core−shell structure is favorable to the improvement of photocatalytic performance.

3.3. Light Absorption Property. UV−vis diffuse reflectance spectroscopy (DRS) was employed to characterize the light absorption properties of CdS and different CdS@SnO_2 samples. As shown in Figure 5, the absorption curves of CdS@SnO_2 composite exhibit a red-shift at the bottom portion compared to the pure CdS NRs. Because SnO_2 cannot absorb visible light because of its wide band gap, the red-shift of absorption for CdS@SnO_2 composite is probably relative to the modification of SnO_2 shell layer. According to previous reports,[43−47] the enhancement of visible light absorption is probably due to following reasons: First, an increase in the local refractive index of the surrounding medium for CdS NRs after replacing air with SnO_2 shell may result in such shift.[43,44] Second, the growth of SnO_2 shell will put pressure on the CdS core. Under shell-induced strain, the band gap of CdS should decrease, and therefore, the absorption shifts to long wavelength direction.[45] Third, the red shift of the spectrum is a typical characteristic of core−shell nanocrystals, originating from the lowering of exciton confinement energy after the core nanocrystals were capped by a higher band gap shell.[46,47]

3.4. Photocatalytic Activity and Photostability. The photocatalytic performances of as-synthesized CdS and different CdS@SnO_2 samples were evaluated by the selective oxidation of BA to BAD under visible-light irradiation (λ > 420 nm). Figure 6 presents the BA conversion rates, BAD yields, and reaction selectivities over different photocatalyst samples after visible light irradiation for 8 h. It can be seen that both BA conversion rate and BAD yield gradually improve with increasing the content of SnO_2 at the beginning, and then have a downtrend after the optimum SnO_2 content of 15%. Especially, the BA conversion rate and BAD yield over CdS@15%SnO_2 are nearly 2 times higher than those over pure CdS. As for the reactive selectivity from BA to BAD, it can be seen that CdS and different CdS@SnO_2 samples have no evident difference (~90%). We further investigated the photocatalytic activity of mechanically mixed CdS−15%SnO_2 which has the same SnO_2 content as CdS@15%SnO_2. As shown in Figure S4 (Supporting Information), the photocatalytic activity of the mixing CdS−15%SnO_2 is obviously higher than CdS but far

DOI: 10.1021/acsami.5b04128
ACS Appl. Mater. Interfaces 2015, 7, 13849−13858

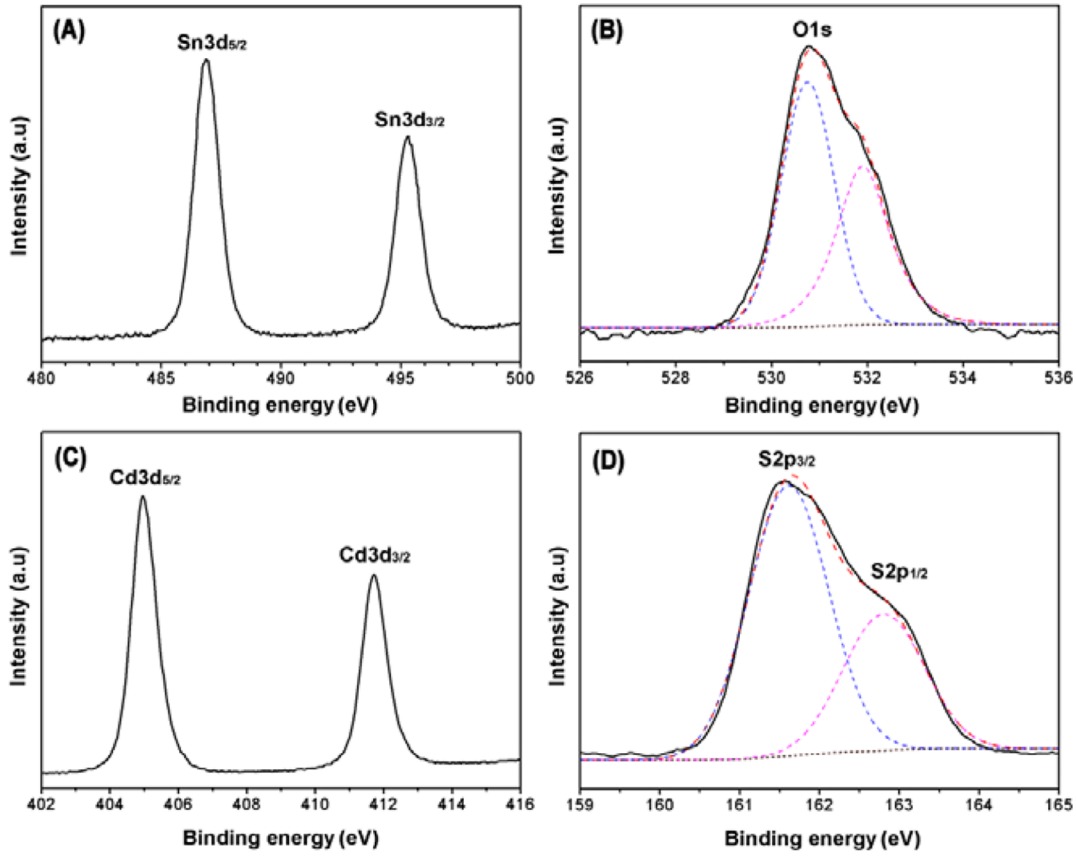

Figure 3. High-resolution XPS spectra of (A) Sn 3d, (B) O 1s, (C) Cd 3d, and (D) S 2p of CdS@15%SnO_2.

lower than the conversion rate over CdS@15%SnO_2. For sample CdS−15%SnO_2, some SnO_2 QDs may be adsorbed on the surface of CdS NRs in the photocatalytic reaction, leading to the improvement of photocatalytic activity in a certain extent. However, both the SnO_2 loading amount and the compact degree between CdS and SnO_2 are probably far lower than those in core−shell structural CdS@15%SnO_2. Consequently, the photocatalytic activity of the mechanically mixed CdS−15%SnO_2 falls between the two other samples.

It is well-known that CdS is prone to taking place photocorrosion, which usually shortens its service life in the photocatalytic applications. Some studies have reported that coating the stable metal oxide semiconductors such as ZnO, TiO_2, and Nb_2O_5 can effectively inhibit the photocorrosion of CdS.[48−51] Here, we investigated the influence of SnO_2 shell layer on the photostability of CdS NRs by recycle photocatalytic experiments and Cd ion leaching tests. Figure S5 (Supporting Information) shows the BAD yields of four recycle runs over CdS and CdS@15% SnO_2. After four recycle runs, the loss percentage of BAD yield over core−shell structural CdS@15%SnO_2 is 27.1%, which is much lower than that over CdS NRs (52.5%). The leaching amounts of Cd ions during the reaction toward CdS and CdS@15% SnO_2 were obtained by measuring the Cd ion concentrations with ICP-AES. From Table S1 (Supporting Information), it can be seen that the leaching amounts of Cd ions toward CdS@SnO_2 is far lower than that toward CdS. The results of the recycle experiments and Cr leaching test indicated that covering the SnO_2 shell layer can effectively improve the photostability of CdS. However, it should be pointed out that loading SnO_2 shell layer is still hard to completely solve the problem of CdS photocorrosion. Solving this problem probably needs the cooperation of other strategies, such as utilizing sacrificial scavengers,[52,53] combing with other semiconductor with higher valence band position,[54,55] confining CdS clusters in porous supports,[56] and so on.

3.5. Photocatalytic Mechanism. It is well-known that the photocatalytic performance of a photocatalyst is closely relative to its light absorption ability, specific surface area, and photogenerated charge separation efficiency.[31,57,58] As shown in Figure 6, the photocatalytic activity of CdS@15%SnO_2 is nearly 2 times higher than that over pure CdS. However, as illustrated in Figure 5, their light absorption properties in the visible region have no evident difference. On the other hand, as displayed in Table 1, although the specific surface area of CdS@SnO_2 has an increasing trend with the increase of SnO_2 content, the variation trend of photocatalytic activity is not always consistent with the change of specific surface area. So, the improvement of photocatalytic activity for CdS@SnO_2 composites cannot be assigned only to the influence of light absorption property and specific surface area. Thus, the result that CdS@SnO_2 composite exhibits higher photocatalytic activity than pure CdS is probably ascribed to the core−shell structure of CdS@SnO_2 composite, by which the photogenerated electrons and holes can be effectively separated. Here, we use transient photocurrent and PL spectrum analyses to identify the influence of core−shell composite structure on charge separation.

Figure 7A shows the photocurrent−time (I−t) curves of CdS and CdS@15%SnO_2 with typical on−off cycles of intermittent visible light irradiation ($\lambda > 420$ nm). The photocurrent boosts rapidly once the light is turned on and remains a relative

DOI: 10.1021/acsami.5b04128
ACS Appl. Mater. Interfaces 2015, 7, 13849−13858

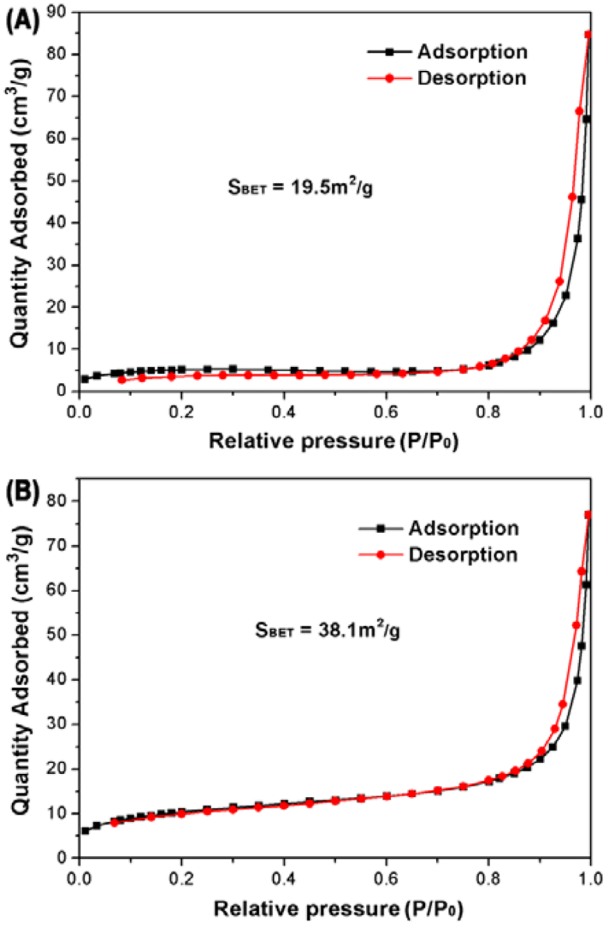

Figure 4. N_2 adsorption−desorption isotherms of (A) CdS NRs and (B) CdS@15%SnO_2 NRs.

Table 1. S_{BET} and Pore Sizes of CdS and Different CdS@SnO_2 Samples

sample	$3S_{BET}$ (m^2g^{-1})	pore size (nm)
CdS	19.5	26.9
CdS@5%SnO_2	20.6	16.5
CdS@10%SnO_2	29.7	14.1
CdS@15%SnO_2	38.1	12.5
CdS@20%SnO_2	47.0	9.8
CdS@25%SnO_2	57.6	7.7

constant value while the light is on. It instantaneously declines to zero when the light is turned off. It has been considered that the initial current is due to the separation of electron−hole pairs at the semiconductor/electrolyte interface: holes are trapped by the reduced species in the electrolyte, while electrons are transported to the back contact substrate.[36,43] From Figure 7A, it can be seen that the core−shell structural CdS@15%SnO_2 exhibits much higher photocurrent than pure CdS, implying that the CdS@SnO_2 core−shell structure possesses higher separation efficiency for the photogenerated electron−hole pairs. This result can be explained by the staggered band gap offset between the two semiconductors: because the conduction and valence band edges of CdS are respectively higher than those of SnO_2, the electrostatic potential gradient across the interface tends to rapidly separate electrons and holes to different sides of the composite, favorable to reducing the combination of electron−hole pairs.

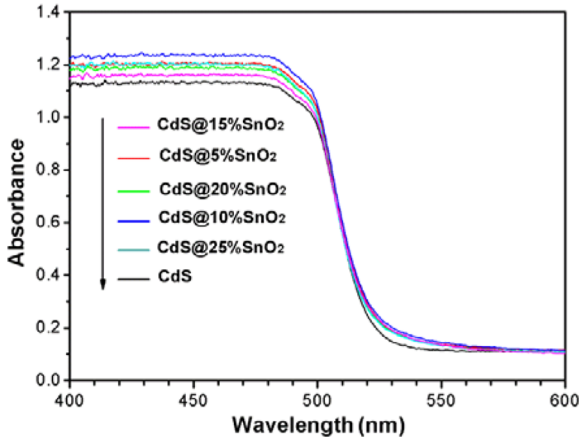

Figure 5. UV−vis DRS spectra of CdS and different CdS@SnO_2 samples.

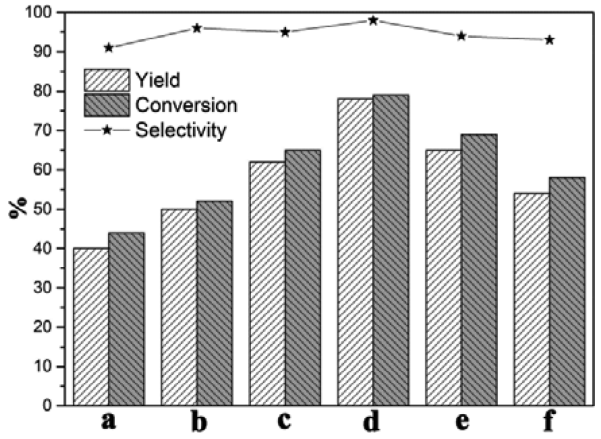

Figure 6. Photocatalytic oxidation of BA to BAD over CdS and different CdS@SnO_2 samples under visible light irradiation (λ > 420 nm): (a) CdS; (b) CdS@5%SnO_2; (c) CdS@10%SnO_2; (d) CdS@15%SnO_2; (e) CdS@20%SnO_2; (f) CdS@25%SnO_2.

As a result, the core−shell structural CdS@SnO_2 shows higher photocatalytic performances when compared to the single CdS.

Because PL emission mainly results from the recombination of free carriers, PL spectrum has been considered to be a useful technique to investigate the efficiency of charge carrier trapping, migration and transfer, and the lifetime of the photogenerated charge carriers in semiconductor particles.[59,60] Figure 7B shows the PL spectra of CdS and core−shell structural CdS@15%SnO_2, obtained at room temperature with an excitation wavelength of 403 nm. Compared to CdS, CdS@15%SnO_2 shows a significant quenching in the photoluminescence emission, indicating the electrons and holes in CdS@15%SnO_2 have been more efficiently separated. This conclusion can be further confirmed by room-temperature TRPL decay analysis. As shown in Table 2, the core−shell structural CdS@15%SnO_2 exhibits a longer PL lifetime (0.462 ns) than the pure CdS (0.267 ns), revealing that the core−shell structure is more favorable to carrier transport.

The reasons for the markedly enhanced photocatalytic performances of core−shell structural CdS@SnO_2 could be explained as follows: First, SnO_2 shell layer can evidently increase the specific surface area, favorable to the adsorption of oxygen and reactants. Second, SnO_2 shell layer can enhance the visible light absorption of CdS in a certain extent. From the

DOI: 10.1021/acsami.5b04128
ACS Appl. Mater. Interfaces 2015, 7, 13849−13858

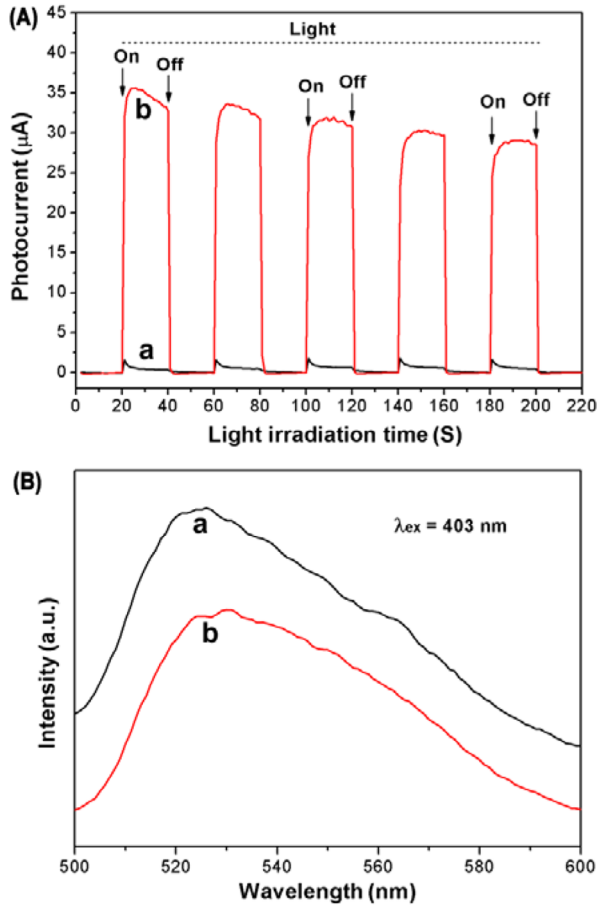

Figure 7. (A) Transient photocurrents of (a) CdS and (b) CdS@15% SnO_2 under visible light irradiation. (B) PL spectra of (a) CdS and (b) CdS@15%SnO_2.

perspective of geometry, the SnO_2 particles dispersed on CdS NRs could increase light trapping by multiscattering, increasing the photon utilization efficiency.[14,61] Most important of all, the CdS@SnO_2 core−shell structure can effectively separate the photogenerated electron−hole pairs. This fleet separation could be explained by the formed staggered band alignment between the two semiconductors at the core−shell interface.[62] In this band gap configuration, when electron−hole pairs are generated in CdS NRs under visible light irradiation, the electrons transfer swiftly to the conduction band of SnO_2 via interfaces, while the holes remain in the valence band of CdS, thus restraining the recombination of the photogenerated carriers.

To understand the primary reactive species involved in the selective oxidation of BA over CdS@SnO_2 under visible light irradiation, we performed a series of control experiments under N_2 atmosphere or in the presence of different radical scavengers. Here, benzoquinone (BQ) was introduced to scavenge $\cdot O_2^-$, ammonium oxalate (AO) for h^+, $K_2S_2O_8$ for e^-, and *t*-BuOH for ·OH in the solution.[63−65] As shown in Figure 8, in N_2 atmosphere, the conversion of BA can be ignored,

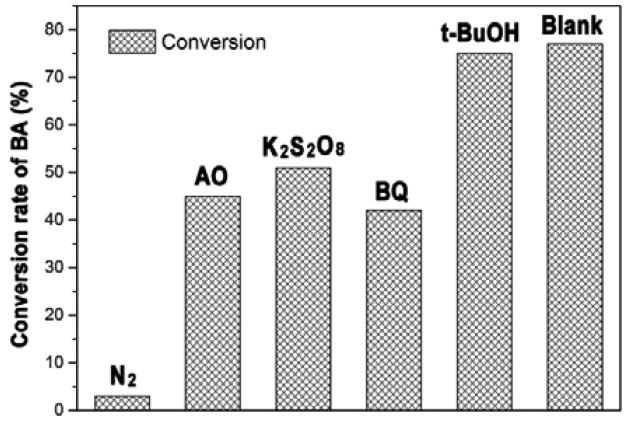

Figure 8. BA conversion rates over CdS@15%SnO_2 under N_2 atmosphere or in the presence of different radical scavengers after visible light irradiation for 8 h.

implying that oxygen is an essential oxidant substance in the photocatalytic oxidation of BA. The additions of $K_2S_2O_8$ and BQ drastically decrease the conversion rate of BA, indicating that $\cdot O_2^-$ is an important reactive species for BA oxidation. A similar inhibition effect is observed with the introduction of AO, manifesting that the photogenerated holes are also involved in the oxidation of BA. There are many stacked pores in SnO_2 shell layer so that BA molecules can easily pass through these pores and further react with the holes on CdS core. However, the addition of t-butanol almost has no influence on the conversion rate of BA, proving that ·OH is not the reactive species for BA oxidation. This is because the reactions were carried out in acetonitrile solution and ·OH radicals cannot be produced. Based on the above experiment results, we can deduce that in this reaction system $\cdot O_2^-$ and hole are the main reactive species for BA oxidation. Additionally, it is well-known that ·OH radicals are nonselective species during photocatalysis process.[66] Thus, the absence of ·OH in this reaction system may be another import reason for obtaining high selectivity.

On the basis of the above experiment results, a plausible mechanism for photocatalytic oxidation of BA over the core−shell structural CdS@SnO_2 NRs is proposed and illustrated in Figure 9. Under visible light irradiation, the electrons are excited from the valence band (VB) of CdS to its conduction band (CB) and rapidly transfer to the CB of SnO_2 owing to their matching energy band positions and close contact. Thus, the electrons concentrate on SnO_2 while holes remain on CdS, favorable to separation of electrons and holes. Subsequently, the electrons would be trapped by the adsorbed oxygen to form $\cdot O_2^-$ radicals. Both $\cdot O_2^-$ radicals and holes take part in the oxidation reaction from BA to BAD.

In addition, we propose a plausible explanation to clarify the influence of SnO_2 content on the photocatalytic properties. The surface of the CdS NRs cannot be entirely covered by SnO_2 until the addition amount of SnO_2 reaches 15%. Thus, increasing the additional amount of SnO_2 can increase the contact area between CdS and SnO_2, favorable to the more

Table 2. PL Lifetimes of CdS and CdS@15%SnO_2 Determined by TRPL Decay Analysis

sample	τ_1 (ns; f_1)	τ_2 (ns; f_2)	T (ns)	fit parameter (χ^2)
CdS	0.06 (0.9418)	3.61 (0.0582)	0.267	1.178
CdS@15%SnO_2	0.08 (0.9029)	4.01 (0.0971)	0.462	1.108

DOI: 10.1021/acsami.5b04128
ACS Appl. Mater. Interfaces 2015, 7, 13849−13858

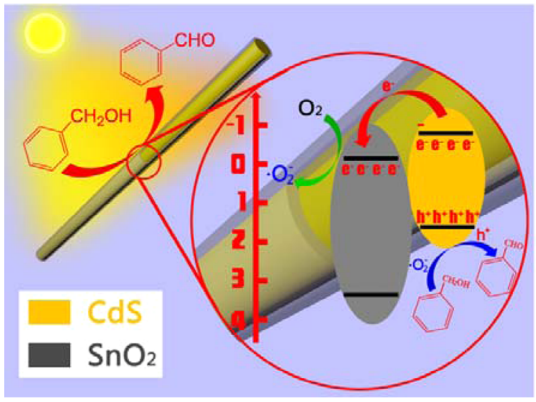

Figure 9. Proposed reaction mechanism from BA to BAD over CdS@SnO_2 photocatalyst.

efficient separation of electron−hole pairs. Consequently, the photocatalytic activity increases with the increase of SnO_2 addition amount. However, when the addition amount is beyond 15%, the photocatalytic activity of CdS@SnO_2 shows a downtrend instead due to the excessively thick SnO_2 shell. This phenomenon may be ascribed to the following reasons: First, the excessively thick SnO_2 shell will restrain the transfer of reactants toward CdS surface. As a consequence, the holes produced in CdS cannot totally participate in the oxidation reaction, resulting in the decline of photocatalytic activity. Moreover, it should be noticed that only CdS core can absorb visible light in core−shell structural CdS@SnO_2. Thus, the excessively thick SnO_2 shell layer also block the transmission of visible light, which further decrease the photocatalytic activity.

4. CONCLUSIONS

In summary, we developed a facile route for fabricating core−shell structural CdS@SnO_2 nanorods, in which SnO_2 nanoparticles were synthesized by a solvent assisted interfacial reaction and further anchored on the surface of CdS nanorods. The thickness of SnO_2 shells can be conveniently adjusted by simply changing the additional amount of SnO_2 nanoparticles. The SnO_2 shell layer has been found to have multiple functions: increasing specific surface area, enhancing visible light absorption, and facilitating the separation of photogenerated charges. Compared with the single CdS NRs, the core−shell structural CdS@SnO_2 exhibited remarkably enhanced photocatalytic activity and improved stability for selective oxidation of benzyl alcohol to benzaldehyde under visible light irradiation. It was revealed that in acetonitrile solution, $\cdot O_2^-$ and holes are the main reactive species responsible for benzyl alcohol to benzaldehyde transformation and the lack of ·OH radicals is favorable to obtaining high reaction selectivity. The synthetic route reported here can potentially be used to synthesize other core−shell structural photocatalysts for green organic syntheses and other photocatalytic applications.

■ ASSOCIATED CONTENT

Supporting Information

EDS spectrum of CdS@15%SnO_2, SAED pattern of CdS nanorod, XRD pattern of SnO_2, conversion rates of BA and yields of BAD over different photocatalysts, recycle testing, and leaching amounts of Cd ions. The Supporting Information is available free of charge on the ACS Publications website at DOI: 10.1021/acsami.5b04128.

■ AUTHOR INFORMATION

Corresponding Authors

*Tel.: +86 21 64252062. Fax: +86 21 64252062. E-mail: baozhutian@ecust.edu.cn.
*E-mail: jlzhang@ecust.eau.cn.

Notes

The authors declare no competing financial interest.

■ ACKNOWLEDGMENTS

This work has been supported by the National Natural Science Foundation of China (21277046, 21173077, 21377038, 21237003), the Shanghai Committee of Science and Technology (13NM1401000), the National Basic Research Program of China (973 Program, 2013CB632403), the Research Fund for the Doctoral Program of Higher Education (20120074130001), and the Fundamental Research Funds for the Central Universities.

■ REFERENCES

(1) Hirakawa, T.; Kamat, P. V. Charge Separation and Catalytic Activity of Ag@TiO_2 Core−Shell Composite Clusters under UV−Irradiation. *J. Am. Chem. Soc.* **2005**, *127*, 3928−3934.
(2) Tian, B. Z.; Wang, T. T.; Dong, R. F.; Bao, S. Y.; Yan, F.; Zhang, J. L. Core-Shell Structured γ-Fe_2O_3@SiO_2@AgBr:Ag Composite with High Magnetic Separation Efficiency and Excellent Visible Light Activity for Acid Orange 7 Degradation. *Appl. Catal., B* **2014**, *147*, 22−28.
(3) Lee, D. C.; Robel, I.; Pietryga, J. M.; Klimov, V. I. Infrared-Active Heterostructured Nanocrystals with Ultralong Carrier Lifetimes. *J. Am. Chem. Soc.* **2010**, *132*, 9960−9962.
(4) Zhang, N.; Liu, S. Q.; Xu, Y. J. Recent Progress on Metal Core@Semiconductor Shell Nanocomposites as a Promising Type of Photocatalyst. *Nanoscale* **2012**, *4*, 2227−2238.
(5) Khanchandani, S.; Kundu, S.; Patra, A.; Ganguli, A. K. Shell Thickness Dependent Photocatalytic Properties of ZnO/CdS Core-Shell Nanorods. *J. Phys. Chem. C* **2012**, *116*, 23653−23662.
(6) Xi, G. C.; Yue, B.; Cao, J.; Ye, J. Fe_3O_4/WO_3 Hierarchical Core-Shell Structure: High-Performance and Recyclable Visible-Light Photocatalysis. *Chem.—Eur. J.* **2011**, *17*, 5145−5154.
(7) Mu, J.; Chen, B.; Zhang, M.; Guo, Z.; Zhang, P.; Zhang, Z.; Sun, Y.; Shao, C.; Liu, Y. Enhancement of the Visible-Light Photocatalytic Activity of In_2O_3−TiO_2 Nanofiber Hetero Architectures. *ACS Appl. Mater. Interface* **2012**, *4*, 424−430.
(8) Wang, X. W.; Yin, L. C.; Liu, G.; Wang, L. Z.; Saito, R.; Lu, G. Q.; Cheng, H. M. Polar Interface-Induced Improvement in High Photocatalytic Hydrogen Evolution over ZnO−CdS Heterostructures. *Energy Environ. Sci.* **2011**, *4*, 3976−3979.
(9) Lee, S.; Lee, K.; Kim, W. D.; Lee, S.; Shin, D. J.; Lee, D. C. Thin Amorphous TiO_2 Shell on CdSe Nanocrystal Quantum Dots Enhances Photocatalysis of Hydrogen Evolution from Water. *J. Phys. Chem. C* **2014**, *118*, 23627−23634.
(10) Chen, Z.; Xu, Y. J. Ultrathin TiO_2 Layer Coated-CdS Spheres Core-Shell Nanocomposite with Enhanced Visible-Light Photoactivity. *ACS Appl. Mater. Interface* **2013**, *5*, 13353−13363.
(11) Liu, S. Q.; Zhang, N. Z.; Tang, R.; Xu, Y. J. Synthesis of One-Dimensional CdS@TiO_2 Core-Shell Nanocomposites Photocatalyst for Selective Redox: The Dual Role of TiO_2 Shell. *ACS Appl. Mater. Interface* **2012**, *4*, 6378−6385.
(12) Zhang, P.; Shao, C. L.; Zhang, Z. Y.; Zhang, M. Y.; Mu, J. B.; Guo, Z. C.; Liu, Y. C. TiO_2@Carbon Core/Shell Nanofibers: Controllable Preparation and Enhanced Visible Photocatalytic Properties. *Nanoscale.* **2011**, *3*, 2943−2949.

DOI: 10.1021/acsami.5b04128
ACS Appl. Mater. Interfaces 2015, 7, 13849−13858

(13) Banerjee, S.; Mohapatra, S. K.; Das, P. P.; Misra, M. Synthesis of Coupled Semiconductor by Filling 1D TiO_2 Nanotubes with CdS. *Chem. Mater.* **2008**, *20*, 6784−6791.
(14) Liu, S. Q.; Yang, M. Q.; Tang, Z. R.; Xu, Y. J. A Nanotree-like CdS/ZnO Nanocomposite with Spatially Branched Hierarchical Structure for Photocatalytic Fine-Chemical Synthesis. *Nanoscale.* **2014**, *6*, 7193−7198.
(15) Liu, C.; Dasgupta, N. P.; Yang, P. Semiconductor Nanowires for Artificial Photosynthesis. *Chem. Mater.* **2014**, *26*, 415−422.
(16) Zhang, Y. L.; Han, C.; Nadagouda, M. N.; Dionysiou, D. The Fabrication of Innovative Single Crystal N,F-Codoped Titanium Dioxide Nanowires with Enhanced Photocatalytic Activity for Degradation of Atrazine. *Appl. Catal., B* **2015**, *168−169*, 550−558.
(17) Hwang, Y. J.; Boukai, A.; Yang, P. D. High Density n-Si/n-TiO_2 Core/Shell Nanowire Arrays with Enhanced Photoactivity. *Nano Lett.* **2009**, *9*, 410−415.
(18) Qin, L.; Pan, X. X.; Wang, L.; Sun, X. P.; Zhang, G. L.; Guo, X. W. Facile Preparation of Mesoporous TiO_2(B) Nanowires with Well-Dispersed Fe_2O_3 Nanoparticles and Their Photochemical Catalytic Behavior. *Appl. Catal., B* **2014**, *150−151*, 544−553.
(19) Wang, D.; Prerre, A.; Kibria, M. G.; Cui, K.; Han, X. G.; Bevan, K. H.; Guo, H.; Paradise, S.; Hakima, A. R.; Mi, Z. Wafer-Level Photocatalytic Water Splitting on GaN Nanowire Arrays Grown by Molecular Beam Epitaxy. *Nano Lett.* **2011**, *11*, 2353−2357.
(20) Hernandez, S.; Cauda, V.; Chiodoni, A.; Dallorto, S.; Sacco, A.; Hidalgo, D.; Celasco, E.; Pirri, C. F. Optimization of 1 D ZnO@TiO_2 Core-Shell Nanostructures for Enhanced Photoelectrochemical Water Splitting under Solar Light Illumination. *ACS Appl. Mater. Interface* **2014**, *6*, 12153−12167.
(21) Zhang, M.; Wang, Q.; Chen, C.; Zang, L.; Ma, W.; Zhao, J. Oxygen Atom Transfer in the Photocatalytic Oxidation of Alcohols by TiO_2: Oxygen Isotope Studies. *Angew. Chem., Int. Ed.* **2009**, *48*, 6081−6084.
(22) Palmisano, G.; Lopez, E. G.; Marci, G.; Loddo, V.; Yurdakal, S.; Augugliaro, V.; Palmisano, L. Advances in Selective Conversions by Heterogeneous Photocatalysis. *Chem. Commun.* **2010**, *46*, 7074−7089.
(23) Tanaka, A.; Hashimoto, K. J.; Kominami, H. Preparation of Au/CeO_2 Exhibiting Strong Surface Plasmon Resonance Effective for Selective or Chemoselective Oxidation of Alcohols to Aldehydes or Ketones in Aqueous Suspensions under Irradiation by Green Light. *J. Am. Chem. Soc.* **2012**, *134*, 14526−14533.
(24) Palmisano, G.; Augugliaro, V.; Pagliaro, M.; Palmisano, L. Photocatalysis: A Promising Route for 21st Century Organic Chemistry. *Chem. Commun.* **2007**, *43*, 3425−3437.
(25) Sheldon, R. A.; Arends, I. W. C. E.; Brink, G. T.; Dijksman, A. Green, Catalytic Oxidations of Alcohols. *Acc. Chem. Res.* **2002**, *35*, 774−781.
(26) Yurdakal, S.; Palmisano, G.; Loddo, V.; Augugliaro, V.; Palmisano, L. Nanostructured Rutile TiO_2 for Selective Photocatalytic Oxidation of Aromatic Alcohols to Aldehydes in Water. *J. Am. Chem. Soc.* **2008**, *130*, 1568−1569.
(27) Schneider, J.; Matsuoka, M.; Takeuchi, M.; Zhang, J. L.; Horiuchi, Y.; Anpo, M.; Bahnemann, D. W. Understanding TiO_2 Photocatalysis: Mechanisms and Materials. *Chem. Rev.* **2014**, *114*, 9919−9986.
(28) Yang, M. Q.; Weng, B.; Xu, Y. J. Synthesis of In_2S_3−CNT Nanocomposites for Selective Reduction under Visible Light. *J. Mater. Chem. A* **2014**, *2*, 1710−1720.
(29) Wang, L.; Wei, H. W.; Fan, Y. J.; Gu, X.; Zhan, J. H. One-Dimensional CdS/α-Fe_2O_3 and CdS/Fe_3O_4 Heterostructures: Epitaxial and Nonepitaxial Growth and Photocatalytic Activity. *J. Phys. Chem. C* **2009**, *113*, 14119−14125.
(30) Lee, K. T.; Lin, C. H.; Lu, S. Y. SnO_2 Quantum Dots Synthesized with a Carrier Solvent Assisted Interfacial Reaction for Band-Structure Engineering of TiO_2 Photocatalysts. *J. Phys. Chem. C* **2014**, *118*, 14457−14463.
(31) Zhang, J. Y.; Wang, Y. H.; Jin, J.; Zhang, J.; Lin, Z.; Huang, F.; Yu, J. G. Efficient Visible Light Photocatalytic Hydrogen Evolution and Enhanced Photostability of Core/Shell CdS/g-C_3N_4 Nanowires. *ACS Appl. Mater. Interfaces* **2013**, *5*, 10317−10324.
(32) Dai, X.; Xie, M.; Meng, S. G.; Fu, X. L.; Chen, S. F. Coupled Systems for Selective Oxidation of Aromatic Alcohols to Aldehydes and Reduction of Nitrobenzene into Aniline Using CdS/g-C_3N_4 Photocatalyst under Visible Light Irradiation. *Appl. Catal., B* **2014**, *158−159*, 382−390.
(33) Sharma, S.; Srivastava, A. K.; Chawla, S. Self-Assembled Surface Adjoined Mesoscopic Spheres of SnO_2 Quantum Dots and Their Optical Properties. *Appl. Surf. Sci.* **2012**, *258*, 8662−8666.
(34) Ghows, N.; Entezari, M. H. Sono-Synthesis of Core-Shell Nanocrystal (CdS/TiO_2) without Surfactant. *Ultrason. Sonochem.* **2012**, *19*, 1070−1078.
(35) Tian, Q. Y.; Wu, W.; Sun, L. L.; Yang, S. L.; Ren, F.; Lei, M.; Zhou, J.; Liu, Y.; Xiao, X. H.; Ren, F.; Jiang, C. Z.; Roy, V. A. L. Tube-like Ternary α-Fe_2O_3@SnO_2@Cu_2O Sandwich Heterostructures: Synthesis and Enhanced Photocatalytic Properties. *ACS Appl. Mater. Interface* **2014**, *6*, 13088−13097.
(36) Gao, T.; Li, Q. H.; Wang, T. H. Sonochemical Synthesis, Optical Properties, and Electrical Properties of Core/Shell-Type ZnO Nanorod/CdS Nanoparticle Composites. *Chem. Mater.* **2005**, *17*, 887−892.
(37) Lee, J. S.; Kwon, O. S.; Jang, J. Facile Synthesis of SnO_2 Nanofibers Decorated with N-Doped ZnO Nanonodules for Visible Light Photocatalysts Using Single-Nozzle Co-electrospinning. *J. Mater. Chem.* **2012**, *22*, 14565−14572.
(38) Cavaliere, S.; Subianto, S.; Savych, I.; Tillard, M.; Jones, D. J.; Roziere, J. Dopant-Driven Nanostructured Loose-Tube SnO_2 Architectures: Alternative Electrocatalyst Supports for Proton Exchange Membrane Fuel Cells. *J. Phys. Chem. C* **2013**, *117*, 18298−18307.
(39) Zhou, G. M.; Wang, D. W.; Li, L.; Li, N.; Li, F.; Cheng, H. M. Nanosize SnO_2 Confined in The Porous Shells of Carbon Cages for Kinetically Efficient and Long-Term Lithium Storage. *Nanoscale* **2013**, *5*, 1576−1582.
(40) Kim, Y. S.; Kim, H. B.; Jang, D. J. Facile Microwave Fabrication of CdS Nanobubbles with Highly Efficient Photocatalytic Performances. *J. Mater. Chem. A* **2014**, *2*, 5791−5799.
(41) Jiang, W. Q.; Zhou, Y. F.; Zhang, Y. L.; Xuan, S. H.; Gong, X. L. Superparamagnetic Ag@Fe_3O_4 Core−Shell Nanospheres: Fabrication, Characterization, and Application as Reusable Nanocatalysts. *Dalton. Trans.* **2012**, *41*, 4594−4601.
(42) Zhou, L.; Wang, W. Z.; Xu, H. L.; Sun, S. M.; Shang, M. Bi_2O_3 Hierarchical Nanostructures: Controllable Synthesis, Growth Mechanism, and Their Application in Photocatalysis. *Chem.—Eur. J.* **2009**, *15*, 1776−1782.
(43) Feng, J.; Wang, Z. F.; Shen, B.; Zhang, L. M.; Yang, X.; He, N. Y. Effects of Template Removal on Both Morphology of Mesoporous Silica-Coated Gold Nanorod and Its Biomedical Application. *RSC Adv.* **2014**, *4*, 28683−28690.
(44) Oldfield, G.; Ung, T.; Mulvaney, P. Au@SnO_2 Core−Shell Nanocapacitors. *Adv. Mater.* **2000**, *12*, 1519−1522.
(45) Chen, X. B.; Lou, Y. B.; Samia, A. C.; Burda, C. Coherency Strain Effects on the Optical Response of Core/Shell Heteronanostructures. *Nano Lett.* **2003**, *3*, 799−803.
(46) Cao, Y. W.; Banin, U. Growth and Properties of Semiconductor Core/Shell Nanocrystals with InAs Cores. *J. Am. Chem. Soc.* **2000**, *122*, 9692−9702.
(47) Lei, C.; Zhang, H.; Hu, J.; Jie, M.; Zhu, H.; Yang, B. Application of Ultrasonic Irradiation in Aqueous Synthesis of Highly Fluorescent CdTe/CdS Core−Shell Nanocrystals. *J. Phys. Chem. C* **2007**, *111*, 2465−2469.
(48) Yang, G. R.; Yan, W.; Zhang, Q.; Shen, S. H.; Ding, S. J. One-Dimensional CdS/ZnO Core/Shell Nanofibers via Single-Spinneret Electrospinning: Tunable Morphology and Efficient Photocatalytic Hydrogen Production. *Nanoscale* **2013**, *5*, 12432−12439.
(49) Yu, K. H.; Lin, X.; Lu, G. H.; Wen, Z. H.; Yuan, C.; Chen, J. H. Optimized CdS Quantum Dot-Sensitized Solar Cell Performance

DOI: 10.1021/acsami.5b04128
ACS Appl. Mater. Interfaces 2015, 7, 13849−13858

Through Atomic Layer Deposition of Ultrathin TiO_2 Coating. *RSC Adv.* **2012**, *2*, 7843−7848.
(50) Wu, L. P.; Zhang, Y. L.; Li, X. J.; Cen, C. P. CdS Nanorod Arrays with TiO_2 Nano-Coating for Improved Photostability and Photocatalytic Activity. *Phys. Chem. Chem. Phys.* **2014**, *16*, 15339−15345.
(51) Pareeek, A.; Paik, P.; Borse, P. H. Nanoniobia Modification of CdS Photoanode for an Efficient and Stable Photoelectrochemical Cell. *Langmuir* **2014**, *30*, 15540−15549.
(52) Cao, S.; Chen, Y.; Wang, C. J.; Lv, X. J.; Fu, W. F. Spectacular Photocatalytic Hydrogen Evolution Using Metal-Phosphide/CdS Hybrid Catalysts under Sunlight Irradiation. *Chem. Commun.* **2015**, *51*, 8708−8711.
(53) Wu, K. F.; Chen, Z. Y.; Lv, H. J.; Zhu, H. M.; Hill, C. L.; Lian, T. Q. Hole Removal Rate Limits Photodriven H_2 Generation Efficiency in CdS-Pt and CdSe/CdS-Pt Semiconductor Nanorod−Metal Tip Heterostructures. *J. Am. Chem. Soc.* **2014**, *136*, 7708−7716.
(54) Wang, P.; Zhang, J.; He, H. L.; Xu, X. L.; Jin, Y. D. Efficient Visible Light-Driven H_2 Production in Water by CdS/CdSe Core/Shell Nanocrystals and an Ordinary Nickel−Sulfur Complex. *Nanoscale* **2014**, *6*, 13470−13475.
(55) Fu, J.; Chang, B. B.; Tian, Y. L.; Xi, F. N.; Dong, X. P. Novel C_3N_4−CdS Composite Photocatalysts with Organic−Inorganic Heterojunctions: In Situ Synthesis, Exceptional Activity, High Stability, and Photocatalytic Mechanism. *J. Mater. Chem. A* **2013**, *1*, 3083−3090.
(56) Peng, R.; Wu, C. M.; Baltrusaitis, J.; Dimitrijevic, N. M.; Rajh, T.; Koodali, R. T. Ultra-stable CdS Incorporated Ti-MCM-48 Mesoporous Materials for Efficient Photocatalytic Decomposition of Water under Visible Light Illumination. *Chem. Commun.* **2013**, *49*, 3221−3223.
(57) Tian, B. Z.; Dong, R. F.; Zhang, J. M.; Bao, S. Y.; Yang, F.; Zhang, J. L. Sandwich-Structured AgCl@Ag@TiO_2 with Excellent Visible-Light Photocatalytic Activity for Organic Pollutant Degradation and *E. coli* K12 Inactivation. *Appl. Catal., B* **2014**, *158−159*, 76−84.
(58) Kudo, A.; Miseki, Y. Heterogeneous Photocatalyst Materials for Water Splitting. *Chem. Soc. Rev.* **2009**, *38*, 253−278.
(59) Weng, B.; Liu, S. Q.; Zhang, N.; Tang, Z. K.; Xu, Y. J. A simple yet Efficient Visible-Light-Driven CdS Nanowires−Carbon Nanotube 1D−1D Nanocomposite Photocatalyst. *J. Catal.* **2014**, *309*, 146−155.
(60) Tian, B. Z.; Li, C. Z.; Gu, F.; Jiang, H. B. Synergetic Effects of Nitrogen Doping and Au Loading on Enhancing the Visible-Light Photocatalytic Activity of Nano-TiO_2. *Catal. Commun.* **2009**, *10*, 925−929.
(61) Xu, X.; Yang, G. R.; Liang, J.; Ding, S. J.; Tang, C. L.; Yang, H. H.; Yan, W.; Yang, G. D.; Yu, D. M. Fabrication of One-Dimensional Heterostructured TiO_2@SnO_2 with Enhanced Photocatalytic Activity. *J. Mater. Chem. A* **2014**, *2*, 116−122.
(62) Niu, M. T.; Huang, F.; Cui, L. F.; Huang, P.; Yu, Y. L.; Wang, Y. S. Hydrothermal Synthesis, Structural Characteristics, and Enhanced Photocatalysis of SnO_2/α-Fe_2O_3 Semiconductor Nanoheterostructures. *ACS Nano* **2010**, *4*, 681−688.
(63) Liu, S. Q.; Yang, M. Q.; Xu, Y. J. Surface Charge Promotes the Synthesis of Large, Flat Structured Graphene-(CdS nanowire)-TiO_2 Nanocomposites as Versatile Visible Light Photocatalysts. *J. Mater. Chem. A* **2014**, *2*, 430−440.
(64) Huang, Y. C.; Li, H.; Balogun, M. S.; Liu, W. Y.; Tong, Y. X.; Lu, X. H.; Ji, H. B. Oxygen Vacancy Induced Bismuth Oxyiodide with Remarkably Increased Visible-Light Absorption and Superior Photocatalytic Performance. *ACS Appl. Mater. Interface* **2014**, *6*, 22920−22927.
(65) Qin, N.; Liu, Y. H.; Wu, W. M.; Shen, L. J.; Chen, X.; Li, Z. H.; Wu, L. One-Dimensional CdS/TiO_2 Nanofibers Composites as Efficient Visible-Light-Driven Photocatalysts for Selective Organic Transformation: Synthesis, Characterization and Performance. *Langmuir* **2015**, *31*, 1203−1209.
(66) Zhang, N.; Yang, M. Q.; Tang, Z. R.; Xu, Y. J. Toward Improving the Graphene-Semiconductor Composite Photoactivity via the Addition of Metal Ions as Generic Interfacial Mediator. *ACS Nano* **2014**, *8*, 623−633.

DOI: 10.1021/acsami.5b04128
ACS Appl. Mater. Interfaces 2015, 7, 13849−13858